ENGINEERING

Dynamic interphase–mediated assembly for deep cycling metal batteries

Weidong Zhang[1,2]†, Qing Zhao[3]†‡, Yunpeng Hou[1], Zeyu Shen[1,2], Lei Fan[1,2], Shaodong Zhou[1], Yingying Lu[1,2]*, Lynden A. Archer[3,4]*

Secondary batteries based on earth-abundant, multivalent metals provide a promising path for high energy density and potentially low-cost electricity storage. Poor anodic reversibility caused by disordered metal crystallization during battery charging remains a fundamental, century-old challenge for the practical use of deep cycling metal batteries. We report that dynamic interphases formed by anisotropic nanostructures dispersed in a battery electrolyte provide a general method for achieving ordered assembly of metal electrodeposits and high anode reversibility. Interphases formed by anisotropic graphitic carbon nitride nanostructures in colloidal electrolytes are shown to promote formation of vertically aligned and spatially compact (~100% compactness) zinc electrodeposits with unprecedented, high levels of reversibility (>99.8%), even at quite high areal capacity (6 to 20 milliampere hour per square centimeter). It is also reported that the same concept enables uniform growth of compact magnesium and aluminum electrodeposits, defining a general pathway toward energy-dense metal batteries based on earth-abundant anode chemistries.

INTRODUCTION

The steadily growing global energy storage market is driving demand for innovative science and technology solutions that enable high-performance and economical batteries, beyond the capabilities of state-of-the-art lithium-based technology (*1*–*3*). Batteries based on multivalent redox chemistries (including Zn/Zn^{2+}, Mg/Mg^{2+}, Al/Al^{3+}, etc.) at the anode have long been heralded as the next generation of energy storage technology solutions because of their ultrahigh theoretical capacity and abundant natural supply of the raw materials (*4*–*6*). A large and growing body of work has shown, however, that irrespective of their chemistry, all metal anodes are plagued by the propensity of metals to crystallize at planar electrodes in loose, irregular, and extreme cases of dendritic assemblies, which lead to poor reversibility and highly inefficient utilization of the electrochemically active metal anode (*7*–*9*). An additional body of work has shown that randomly oriented electrodeposits with high porosity have strong tendency to become electrically isolated, which also leads to poor reversibility (*10*–*12*).

The interphase generated by chemical and electrochemical transformations between any battery electrode and electrolyte is now understood to play a crucial role in regulating ion transport and electrodeposit morphology at a metal anode (*13*, *14*). Well-designed solid electrolyte interphases (SEIs) in lithium batteries are known, for example, to facilitate ion desolvation, to repel free electrolyte molecules at the electrified interface, and to manipulate the local ion transport electrokinetics (*15*–*17*). Preformed SEIs anchored on metal anodes have consequently been reported to be highly effective in tuning the morphologies of metal deposits (*18*–*20*). Unfortunately, at the high anode capacities encountered during deep cycling of practical batteries, the artificial SEIs typically break, enabling electrolyte components to freely access and be reduced by the anode, consuming electrolyte and markedly lowering the anode reversibility. Building a conductive interfacial layer with low lattice mismatch of metal deposits has been reported recently as an effective strategy to achieve compact metal electrodeposition by regulating the epitaxial electrodeposition with preferred facet orientation (*21*, *22*). This interfacial layer is conductive and thus has to be anchored to a substrate. Its influence on electrodeposit morphology decays with distance from the substrate, and as a consequence, the regulation is limited to moderate to low anode capacities (e.g., <5 mA·hour cm^{-2}) (*23*–*25*).

A strategy that would enforcing similar strong constraints on metal crystallization but can be dynamically deployed using freely diffusing agents inside a liquid electrolyte is obviously and potentially far-reaching importance. If the designed interphase can itself assemble and disassemble on time scales that are fast relative to typical metal electrodeposition rates in batteries, then the metal electrodeposit growth can be regulated to arbitrarily high extents. We note that dynamic regulation via interlaminar interphases is a versatile methodology for natural organisms to produce hierarchically structured minerals (*26*). For example, nacres with laminated microstructures can pregenerate layered biopolymeric interphases, as interlaminar templates, to dynamically bind ion precursors and promote oriented crystallization between the biopolymeric interphases (*27*). Dynamic assembly process can also be applied to deposit or mineralize diverse kinds of inorganic crystals with hierarchical superstructures through the delicate interaction between building blocks and designed interphases (*28*, *29*).

In order for dynamic interphases formed inside a battery cell to regulate metal deposition at low or high capacities, the interphase must satisfy at least three criteria: (i) It must be nonconductive to facilitate metal electrodeposition without concern of automatic short circuit; (ii) it must be anisotropic and exhibit preferred orientation under the electric fields; and (iii) it must exhibit strong interaction with specific metal facets to template/direct the deposit growth in a preferred orientation. We choose to study Zn metal anode as the model system due to its already well-known merits including the

[1]State Key Laboratory of Chemical Engineering, College of Chemical and Biological Engineering, Zhejiang University, Hangzhou 310027, China. [2]ZJU–Hangzhou Global Scientific and Technological Innovation Center, Hangzhou 311215, China. [3]Robert Frederick Smith School of Chemical and Biomolecular Engineering, Cornell University, Ithaca, NY 14853, USA. [4]Department of Materials Science and Engineering, Cornell University, Ithaca, NY 14853, USA.
*Corresponding author. Email: yingyinglu@zju.edu.cn (Y.L.); laa25@cornell.edu (L.A.A.)
†These authors contributed equally to this work.
‡Present address: Key Laboratory of Advanced Energy Materials Chemistry (Ministry of Education), College of Chemistry, Nankai University, Tianjin 300071, China.

use of water as the electrolyte solvent, the relatively high volumetric capacity (5855 A·hour liter^{-1} for zinc), in comparison to other anode technologies (e.g., 790 A·hour liter^{-1} for graphite and 2066 A·hour liter^{-1} for lithium), as well as the intrinsic safety and cost efficiency characteristics (*30*–*32*). The higher Young's modulus of zinc (108 GPa) than other metals (Mg, 45 GPa; Al, 69 GPa) at the liquid/solid interface also means that batteries based on Zn have much lower tolerance for nonuniform/noncompact deposition of the metal, as the strong Zn deposits will easily break through any barriers to short-circuit the battery cell (*33*), in addition to driving chemical/electrochemical side reaction toward aqueous electrolytes (*34*, *35*).

We report that dense and vertically aligned Zn electrodeposition can be achieved via dynamic adsorption of artificial interphases formed in a simple colloidal electrolyte containing graphitic C_3N_4 (g-C_3N_4) nanosheets (fig. S1). The g-C_3N_4 nanosheets are of specific interest because of their high crystallographic match for hexagonal close-packed (HCP) Zn and, as will be shown later, can be dynamically adsorbed/desorbed on $(0002)_{Zn}$ facet during the depositing/stripping process. In situ quantitative experiments reveal that the ordered Zn deposits result in a notably decreased consumption of Zn and markedly lower accumulation of by-products during each cycle. These merits result in unprecedented Zn reversibility (~99.8%) and high cumulative capacity (2520 mA·hour cm^{-2}) suitable for practical aqueous Zn metal batteries (AZMB) with areal capacities as high as 20 mA·hour cm^{-2}.

RESULTS AND DISCUSSION

Aligned Zn electrodeposits under dynamic interphase mediation

An improved anode reversibility is associated with the dense and oriented assembly of Zn electrodeposits. It is known that HCP crystallography of Zn plays a central role in Zn electrodeposit growth by facilitating the formation of hexagonal Zn platelets exposing $(0002)_{Zn}$ facet with the lowest surface energy (fig. S2) (*36*). Focused ion beam scanning electron microscopy (FIB-SEM) analysis was carried out to provide insights into the inner microstructural details of Zn growth in aqueous electrolyte (Fig. 1A). Hexagonal Zn platelets with various sizes (1 to 5 μm) are observed to form loosely connected building blocks assembled to create a porous electrodeposit structure in the control materials. The Zn deposits are revealed to be randomly oriented using the reconstructed stack of cross-sectional slices under slice and view modes (Fig. 1B and fig. S3). We hypothesize that the increased surface area associated with these structures exposed in aqueous electrolyte media caused by the irregular interstices inside the bulk deposits is the main cause of uncontrolled interfacial side reactions and poor Zn anode reversibility. In contrast, dense Zn electrodeposits without inner interstices formed in electrolytes containing the g-C_3N_4 (fig. S4) are observed. Hexagonal Zn platelets with uniform size are seen to be vertically stacked together (~100% compactness) and induce a sharp decrease in contact area with aqueous electrolytes (Fig. 1, C and D).

The growth of vertically aligned Zn electrodeposits is triggered by the orientated nanosheets with facet-dependent adsorption ability under the electric field. As shown in Fig. 2A, the critical steps to facilitate the torsion and alignment of nanosheets in aqueous electrolyte are as follows: (i) Electron-donating functional groups on the g-C_3N_4 nanosheets can induce an ordered electric double layer (EDL) in the colloidal electrolyte. (ii) Under the electric field, excess counterions inside the EDL migrate and lead an electro-osmotic flow along the nanosheet surface, inducing an EDL polarization (*37*). Because of the anisotropic structure of nanosheets, excess polarization parallel to nanosheet surface can induce a torque to align the

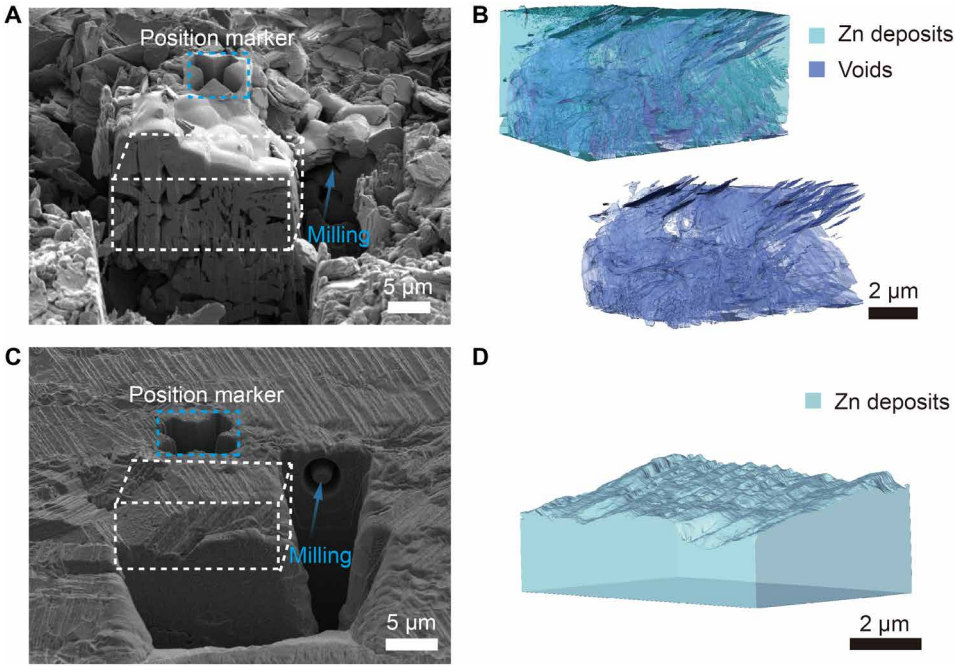

Fig. 1. Densely packed Zn electrodeposits featuring vertically aligned hexagonal platelets. Cross-sectional images produced by FIB and three-dimensional (3D) morphology reconstructions of Zn deposits in (**A** and **B**) control 2 M $ZnSO_4$ (aq) liquid electrolytes. Randomly oriented Zn electrodeposits assemble to form porous and loose microstructures; and (**C** and **D**) aqueous 2 M $ZnSO_4$ colloidal electrolytes prepared through g-C_3N_4 addition. A fixed concentration of g-C_3N_4 of 1.0 mg ml^{-1} was used in these studies. Vertically aligned and dense electrodeposits are observed in the colloidal electrolytes under the dynamic interphase mediation. The current density was 4 mA cm^{-2}.

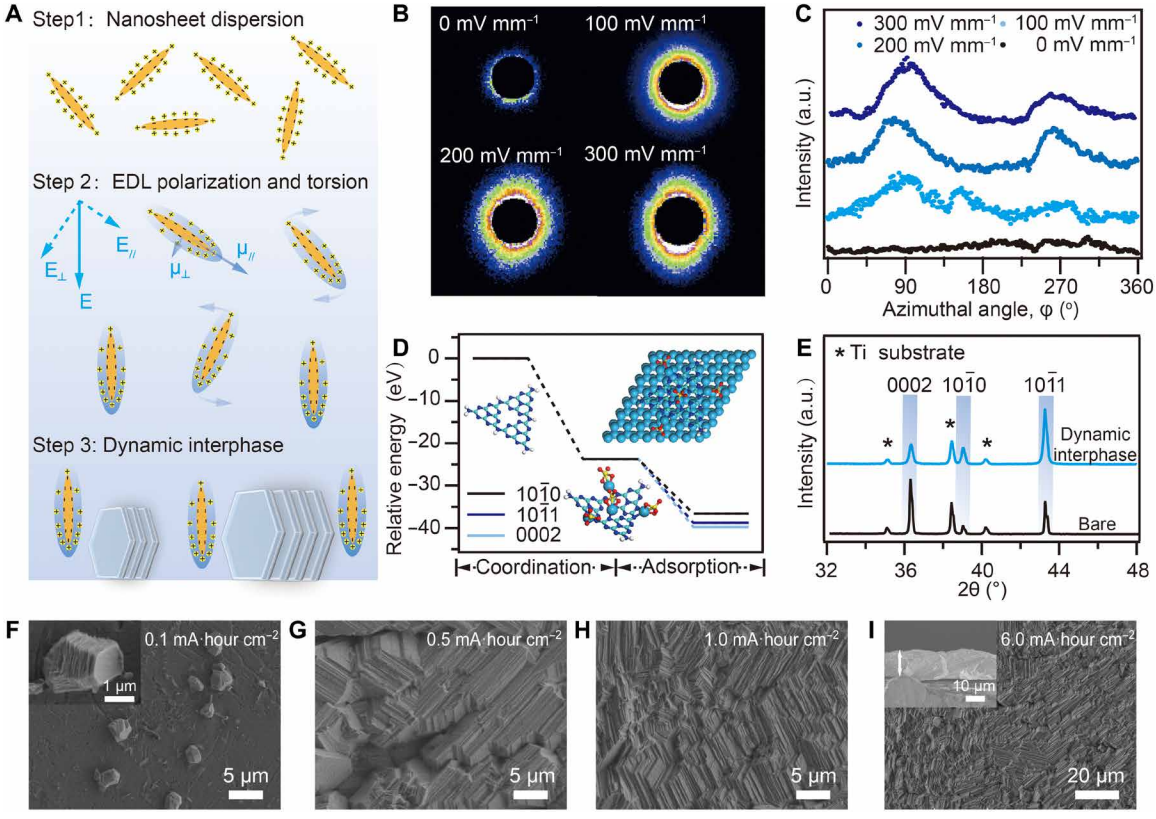

Fig. 2. Oriented interphases and Zn electrodeposits formed under the electric field. (**A**) Schematic of the electro-orientation process. (**B** and **C**) 2D small-angle x-ray scattering (SAXS) images and azimuthal angle (φ) plots reveal the nanosheet distribution at the electrified interface from disordered to aligned structure upon the electric field intensity increased from 0 to 300 mV mm^{-1}. a.u., arbitrary units. (**D**) Free energy diagram of the coordination and adsorption process on different Zn facets. Insets: Ion-coordinated nanosheets preferentially adsorbed on the $(0002)_{Zn}$ facet. (**E**) Crystallographic orientation differences of Zn deposits with or without dynamic interphase mediation. (**F** to **I**) SEM images reveal the nucleation and growth patterns of Zn electrodeposits under dynamic interphase mediation. The current density was 4 mA cm^{-2}.

nanosheets with the electric field (text S1) (*38*). (iii) The vertically aligned nanosheets at the liquid-solid interface can further influence the orientation of Zn electrodeposits by preferential adsorption on $(0002)_{Zn}$ facet.

The electro-orientation of nanosheets in the electrolyte upon applying the electric field can be verified by small-angle x-ray scattering (SAXS) measurements (Fig. 2, B and C). The isotropic scattering pattern and nearly flat azimuthal angle plot of the colloidal dispersion without electric field suggest the random distribution of nanosheets. Stronger equatorial scattering patterns in SAXS images and peak intensity in azimuthal angle plots reflect improved alignment of nanosheets with the increase in electric field intensity. Dynamic adsorption of the artificial interphases on specific exposed facet can further promote the growth of aligned Zn electrodeposits. Free energy diagram is plotted to reveal the ion coordination process and preferential adsorption of g-C_3N_4 nanosheets (Fig. 2D). A unit of g-C_3N_4 can spontaneously adsorb at least four zinc ions and form an ionized nanosheet with high structural symmetry in the aqueous electrolyte. Moreover, density functional theory (DFT) calculations reveal that ionized nanosheets exhibit stronger binding affinity with $(0002)_{Zn}$ facet (−16.05 eV) compared to $(10\bar{1}0)_{Zn}$ or $(10\bar{1}1)_{Zn}$, and thus facet-dependent adsorption encourages the vertical growth of oriented Zn electrodeposits by blocking $(0002)_{Zn}$ facets (fig. S5). To further demonstrate the synergistic effect of electro-oriented interphases and facet-dependent adsorption, we tested Zn electrodeposition using fixed g-C_3N_4 nanosheets parallel to the separator as a comparison (fig. S6). Distinctly different morphologies featuring horizontally aligned Zn electrodeposits can be observed at 1 mA·hour cm^{-2} and become random-oriented at 3 mA·hour cm^{-2} because of the lack of dynamic facet-dependent regulation.

The vertically aligned Zn electrodeposits exhibit a $(10\bar{1}1)$ texture, benchmarking against the random orientation in bare electrolyte (Fig. 2E). The nucleation and growth patterns of Zn electrodeposits under the dynamic interphase mediation were further investigated (Fig. 2, F to H, and fig. S7). Hexagonal Zn platelets cofacially stack and form the uniform distributed nucleus at the nucleation stage, and then ordered crystal coarsening and lateral spreading mediated by electro-oriented interphases can be achieved during the growth stage. Under deep depositing condition with a high capacity of 6 mA·hour cm^{-2}, the thickness of the $(10\bar{1}1)$ textured Zn electrodeposits is 13.79 μm, in sharp contrast to the loose and nonuniform electrodeposits in bare electrolyte (22.25 μm in thickness) (fig. S8). In addition to aqueous electrolytes containing $ZnSO_4$, dynamic interphase–mediated Zn electrodeposition can be readily applied to other aqueous electrolytes of interest, such as $ZnCl_2$, $Zn(OAc)_2$, and $Zn(CF_3SO_3)_2$ (fig. S9).

Dynamic assembly/disassembly of Zn electrodeposits

To clarify the nanoscale spatial structure and chemical information of dynamic interphase over the vertically aligned Zn electrodeposits,

we performed atomic force microscopy–based infrared (AFM-IR) spectroscopy. The localized IR absorption spectra at different sites over the sample can be measured by AFM cantilevers (Fig. 3A), based on the instantaneous thermal expansion stems from local absorption of IR radiation (*39*). The characteristic absorption peak at 1637 cm^{-1} can be assigned to the C═N stretching vibrations, which exhibits an excellent agreement with the spectra of g-C_3N_4 powders measured by conventional Fourier transform IR spectrometer (fig. S10). IR signals with higher intensities at sites 1 and 3 suggested that g-C_3N_4 nanosheets may directly interact with side walls of the Zn electrodeposits. AFM topography image (Fig. 3B) and IR absorption mapping image at 1637 cm^{-1} (Fig. 3C and fig. S11) further reveal the linear distribution of nanosheets correlated with the aligned Zn platelets. A cross-sectional lamellae of aligned Zn deposits were prepared by FIB lift-out method, and a clear crystalline–amorphous crystalline heterogeneous structure can be observed (figs. S12 and S13). The aligned Zn platelets are strongly bounded by intercalated g-C_3N_4 nanosheets (2 to 4 nm in thickness) and stacked to form a dense laminated microstructure.

In situ electrochemical quartz crystal microbalance (EQCM) and cyclic voltammetry (CV) tests were combined to provide a quantitative understanding on dynamic interphase–mediated depositing/stripping behavior (fig. S14). EQCM can precisely monitor the mass changes on the quartz crystal working electrode with a function of potentials applied by CV (*40*). Coulombic efficiency (CE) and mass efficiency (ME), defined as the electron transfer and mass change ratio between Zn stripping and Zn depositing during each cycle, respectively, are introduced to quantitatively monitor the irreversible consumption of active Zn and by-product accumulation. As shown in Fig. 3 (D and E), severe mass accumulation originated from electrochemically inactive Zn (average CE, 90.8%) and by-products (average ME, 48.3%) after stripping repeatedly occurred in bare $ZnSO_4$ electrolyte. However, highly reversible depositing/stripping process with an average CE of 99.6% can be observed under the mediation of dynamic interphase. Side reactions associated with the lack of interfacial protection can be resolved (average ME, 98.5%) because of the existence of the dynamic interphase adsorbed on Zn platelets. Moreover, the weight of intercalated g-C_3N_4 nanosheets in the aligned Zn deposits is approximately 3.28 weight %, which can be quantified on the basis of the value difference between actual mass increase in quartz crystal and the theoretical mass change according to electron transfer numbers in CV (Fig. 3F).

Performance of practical metal batteries

Practical energy-dense AZMB require an extremely high CE to minimize the active Zn loss during each cycle. Long-term CE tests were first carried out in electrochemical cells to assess the utility function of dynamic interphase mediation. At a moderate areal capacity of 1 mA·hour cm^{-2}, the average CE reaches 99.6% over 1600 cycles under the dynamic interphase mediation, while the CE drops below 90% after 160 cycles for bare electrolyte. As shown in Fig. 4B, Zn cyclability was further evaluated under deep cycling

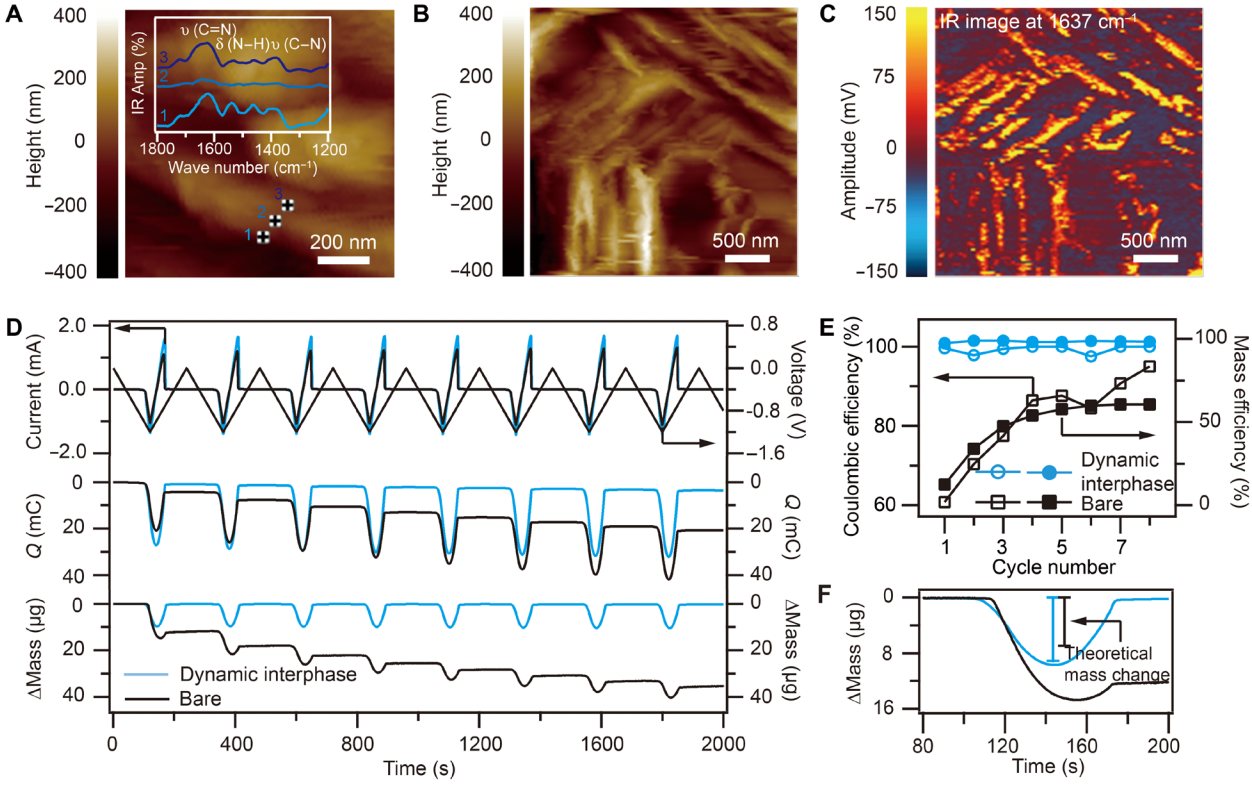

Fig. 3. Dynamic interphase–mediated Zinc anode cycling. (**A**) Localized IR absorption spectra of Zn platelet deposited under dynamic interphase mediation. (**B** and **C**) AFM topography of aligned electrodeposits and the corresponding IR absorption mapping of C═N bond stretching (1637 cm^{-1}). (**D**) Cyclic voltammetry (CV; 0.0 and −1.2 V versus Ag/AgCl), chronocoulometry, and electrochemical quartz crystal microbalance (EQCM) tests to track the depositing/stripping process in different electrolytes at a scan rate of 10 mV s^{-1}. (**E**) Zn plating/stripping Coulombic efficiency (CE) and mass efficiency (ME) in a three-electrode cell based on CV and EQCM. (**F**) Mass changes on quartz crystal electrode during first cycle.

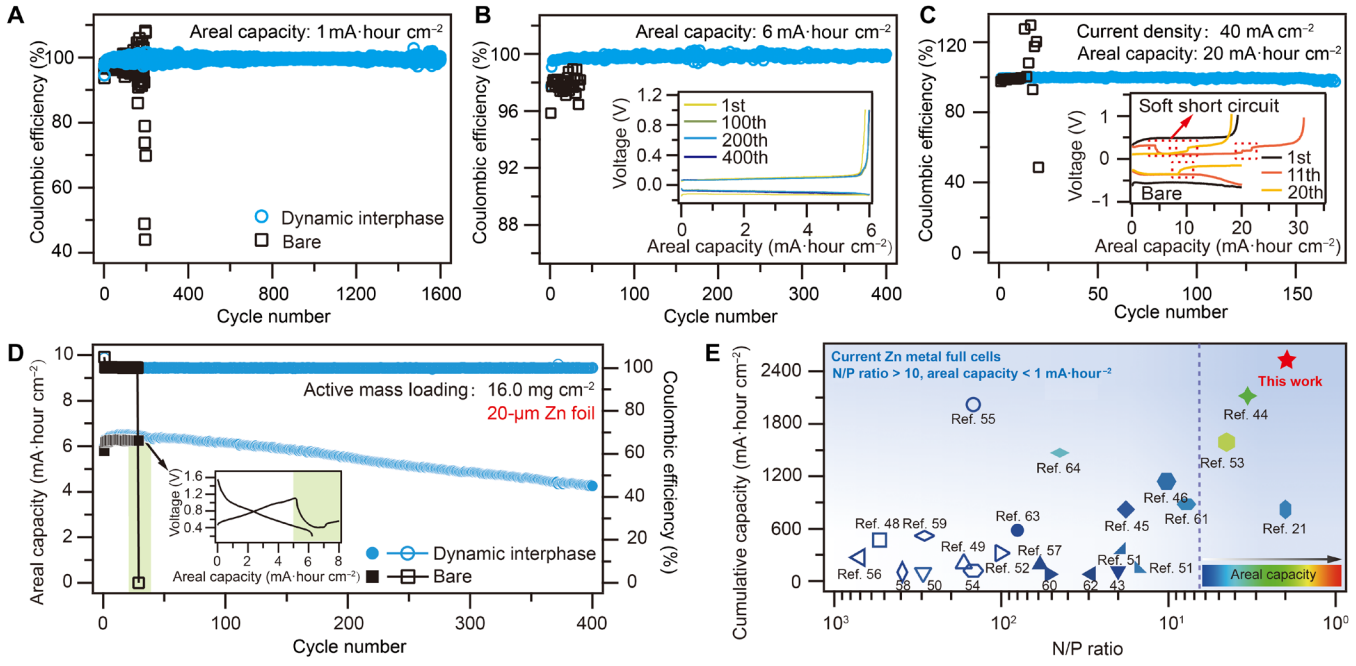

Fig. 4. Electrochemical performance of practical Zn metal batteries mediated by dynamic interphase. (**A** and **B**) Long-term Zn CE tests under shallow cycling conditions (A) and deep cycling conditions (B) at 4 mA cm^{-2}. (**C**) High-efficiency Zn metal deposition/stripping under high current density (40 mA cm^{-2}) and high areal capacity (20 mA·hour cm^{-2}). (**D**) Long-term cycling performance of full cells using 20-μm-thick Zn anodes and high mass loading ZnVO cathodes (6.3 mA·hour cm^{-2}), N/P ratio = 1.85. (**E**) Comparison of the cycling performance of Zn metal full cells with previous reports.

condition (e.g., 6 mA·hour cm^{-2}), which is equivalent to the ideal areal capacity in practical full batteries. Significantly improved CE (averaging 99.8% over 400 cycles) demonstrates the high-efficiency Zn utilization during the vertically aligned depositing/stripping process. By contrast, the cell without modifications short-circuited because of irregular Zn deposits after just 36 cycles. Under the mediation of dynamic interphase, well-maintained Zn reversibility and stable voltage hysteresis can be achieved at various current densities from 1 to 10 mA cm^{-2} (figs. S15 and S16). It is also noteworthy that the CE (average, 99.5%; Fig. 4C and fig. S17) was not compromised under ultrahigh current density (40 mA cm^{-2}) and ultrahigh areal capacity condition (20 mA·hour cm^{-2}).

The superiority of dynamic interphase–mediated high-efficiency Zn depositing/stripping can be further demonstrated in practical full batteries. We note that most of the AZMB reported in literature were tested using huge excess Zn metal anodes (>100 μm in thickness), low mass loading cathodes (<1 mA·hour cm^{-2}), and flooded electrolytes (>100 μl mA·hour^{-1}), which will markedly reduce the actual energy density and conceal the anode challenges in full batteries. From application perspectives, the use of thin Zn anode (<30 μm) under deep cycling conditions (>4 mA·hour cm^{-2}) is the necessary parameters for practical AZMB designs (*24*, *41*). Here, we design the Zn/$Zn_xV_2O_5$ nH_2O (ZnVO) full batteries tested under highly challenging conditions: ultrathin zinc anode (20 μm), high mass loading ZnVO cathode (16 mg cm^{-2}; fig. S18), and lean electrolyte (10 μl mA·hour^{-1}). ZnVO nanobelts with high specific capacity and reversible Zn^{2+} intercalation/deintercalation ability (fig. S19) were chosen as a candidate for cathode materials (*42*). The rational designed negative-to-positive capacity (N/P) ratio of 1.85 and deep cycling condition enable a high energy density of 280 W·hour liter^{-1} (table. S1; based on anode, cathode, and separator). As shown in Fig. 4C, Zn/ZnVO full batteries using bare electrolyte can only run 29 cycles before a sudden internal short circuit, while approximately 13 times longer cycling life span (400 cycles) and continuous operation time (1100 hours) can be achieved via the application of dynamic interphase. Postcycling characterizations of dynamic interphase–mediated Zn anodes reveal that excellent cycling stability of full batteries can be attributed to the high-efficiency and ordered stripping pattern over the vertically aligned electrodeposits (fig. S20). The performance of Zn/ZnVO full batteries under the dynamic interphase mediation is among the best to date for practical AZMB (table S2). Compared with previous literature, our work stands out for the highest cumulative capacity (up to 2520 mA·hour cm^{-2}), highest per-cycle areal capacity (6.3 mA·hour cm^{-2}) and lowest N/P ratio (1.85), providing a promising route for practical AZMB (Fig. 4E).

Dynamic interphase mediation is a versatile strategy for high-capacity metal anodes. Similar to dynamic function of g-C_3N_4 nanosheets in the aforementioned electrochemical cells, boron nitride (BN) nanosheets with high aspect ratio and six-membered ring structure can also work as dynamic interphase to regulate the Zn electrodeposition. EQCM revealed that significantly improved plating/stripping reversibility can also be achieved under the mediation of BN nanosheets (fig. S21). Moreover, this strategy can be readily extended to other energy-dense metal batteries systems. Metallic Mg with the same HCP crystal structure as Zn exhibited a vertically aligned morphology with (10$\bar{1}$1) texture, and an improved CE of 98.6% under the dynamic interphase mediation, in contrast to the nonuniform, random assembled Mg electrodeposits (average CE of 79.9% for control cells), formed in bare electrolytes (fig. S22). We further evaluated the utility of our concept in multivalent Al anodes. As shown in fig. S23, the dynamic interphase provides a large driving force between Al electrodeposit grains, enabling a densely

packed morphology and exceptional reversibility (average CE, 98.74%) at high areal capacity (3 mA·hour cm^{-2}).

In summary, we have developed a dynamic interphase strategy to promote ordered assembly of metal electrodeposits under deep cycling condition. Using Zn anode as an example, exceptionally reversible Zn depositing/stripping (>99.8%) under deep cycling conditions (6 to 20 mA·hour cm^{-2}) can be achieved by the dynamic mediation of artificial interphases. Artificial interphases adsorbed on selective facet can promote cofacially stacked Zn electrodeposits and hinder the electrolyte-related interfacial side reactions. The dynamic interphase concept can be extended to achieve densely assembled Mg and Al electrodeposits in multivalent metal batteries, providing a brand-new route for the development of deep cycling metal batteries.

MATERIALS AND METHODS

Preparation of electrolytes

Zn electrolyte

$ZnSO_4{\cdot}7H_2O$ was dissolved in the deionized water to prepare the 2 M $ZnSO_4$ electrolyte for Zn electrochemical cells.

Mg electrolyte

$AlCl_3$ powder was slowly added into phenyl magnesium chloride tetrahydrofuran solution in an Ar-filled glovebox [<0.1 parts per million (ppm) H_2O and <0.1 ppm O_2].

Al electrolyte

$AlCl_3$ powder was slowly added into [EMIm]Cl (1-ethyl-3-methylimidazolium chloride) in an Ar-filled glovebox. The molar ratio [EMIm]Cl:$AlCl_3$ = 1:1.3.

Preparation of nanosheet suspension

Bulk g-C_3N_4 powder was synthesized by thermal polymerization of melamine. Briefly, 10 g of melamine was placed in a covered crucible and then heated to 550°C for 2 hours in Ar atmosphere with a heating rate of 5°C min^{-1}. The as-prepared powder was further heated at 600°C for 4 hours under air. The g-C_3N_4 nanosheet or BN nanosheet suspensions were fabricated by liquid phase exfoliation of the above bulk powders. Typically, the bulk powder was dispersed in H_2O with a concentration of 5 mg ml^{-1}. The dispersion was sonicated for 6 hours in an ultrasonic cell crusher (700 W), after which the suspension is centrifuged at 4000 rpm for 10 min and gives nanosheets/H_2O suspension with a concentration of ~1.0 mg ml^{-1}.

Preparation of electro-oriented hydrogels

First, 3 g of acrylamide, 15 mg of *N*,*N*′-methylenebis(acrylamide), 15 mg of ammonium persulfate, and 30 μl of *N*,*N*,*N*′,*N*′-tetramethylethylenediamine were sequentially added into 15 ml of 2 M $ZnSO_4$ electrolyte (with ~1.0 mg ml^{-1} of g-C_3N_4 nanosheets). The precursor solution was quickly injected into a glass mold (between two electrodes), and then the cell was charged at 80°C for 30 min. The distance between the electrodes is 1 mm. The obtained hydrogels were rinsed in deionized water and can be used in SAXS tests.

Orientation-confined tests

The g-C_3N_4 nanosheet–coated separator was prepared by a vacuum-assisted infiltration method. g-C_3N_4 nanosheet suspension (~1.0 mg ml^{-1}; with 5% Nafion solution as a binder) was filtrated on a cellulose separator (Shanghai Xinya Purification Equipment Co. Ltd.). The g-C_3N_4 nanosheet–coated separators were dried in a vacuum oven at 60°C for 12 hours. The lamellar membrane with fixed g-C_3N_4 nanosheets were used as separator in the orientation-confined tests.

Material characterization

Field-emission SEM measurements were conducted on Hitachi SU8000. X-ray diffraction (XRD) patterns were obtained using a PANalytical X'Pert Powder with Cu-Kα radiation. SAXS measurements were performed on a Xeuss SAXS system (Xenocs SA). Transmission electron microscopy (TEM) lamella sample was prepared by a dual-beam FIB-SEM (FEI Quanta 3D FEG) with a nanomanipulator, using a standard lift-out procedure. The initial lamella was milled with a Ga ion beam (30 kV and 1 nA) and then mounted on a TEM grid. Thinning was first conducted with a beam current of 500 pA and then final polishing with a beam current of tens of picoamperes to remove amorphization. TEM measurements were performed on JEOL 2100F with a Gatan K2 direct detection camera to identify the crystallography of electrodeposits.

FIB and three-dimensional morphology reconstructions

The cross sections and bulk structures of electrochemically deposited Zn were analyzed by dual-beam SEM (Thermo Fisher Scientific, FIB Helios G3 UC). To maintain the structural integrity of Zn deposits in bare 2 M $ZnSO_4$ during FIB milling, platinum was sputtered on the samples using the gas injection system. A Ga ion beam (30 kV and 0.79 nA) was used to serially section and polish the sample. The data were collected until up to 400 cross-sectional images were captured to provide a full size of Zn deposits. Alignment corrections of the image stack and digital reconstruction three-dimensional (3D) morphology were visualized by IMOD (Boulder Laboratory) and Amira 6.5 (Thermo Fisher Scientific).

AFM-IR spectroscopy measurements

The localized nanoscale mid-IR spectra and absorption maps were carried out using a NanoIR2-fs instrument (Anasys Instruments Inc.) under contact mode. These measurements are based on the photothermal induced resonance of the AFM cantilever. The resonant amplitudes of the AFM cantilever are positively correlated with the absorbed IR radiation of samples. IR spectra were acquired over the 900 to 1900 cm^{-1} with a resolution of 5 cm^{-1}. The AFM-IR spectra and 3D intensity maps were generated using Analysis Studio software for the NanoIR2 system.

Electrochemical quartz crystal microbalance

The zinc deposition/stripping happened in an EQCM cell (QCM922, Princeton Applied Research, USA). The EQCM experiments carried out at a scan rate of 10 mV s^{-1} a specially designed electrolytic cell using a standard three-electrode configuration. A gold-coated quartz crystal electrode, a platinum electrode, and an Ag/AgCl electrode were used respectively as the working electrode, counter electrode, and reference electrode.

The mass change (Δm) of Zn deposits on the quartz surface should follow the Sauerbrey equation

$$\Delta f = -2f_0^2(\mu_q\rho_q)^{-\frac{1}{2}}\Delta m/A$$

Here, Δf is the frequency change, f_0 is the resonant frequency of the quartz crystal (9 MHz), μ_q is the shear modulus of quartz

(2.947×10^{11} g cm^{-1} s^{-2}), ρ_q is the density of quartz (2.648 g cm^{-3}), and A is the piezoelectrically active crystal area (0.196 cm^{-2}).

Preparation of high mass loading $Zn_{0.25}V_2O_5$ cathode

$Zn_{0.25}V_2O_5$ nanobelts were synthesized via a hydrothermal method. Typically, 0.54 g of V_2O_5 and 0.43 g of $Zn(OAc)_2$ were dissolved in a mixed solvent (70 ml of deionized water, 5 ml of acetone, and 2 ml of 10% HNO_3). The autoclave was sealed and heated at 180°C for 24 hours. The as-synthesized product was filtrated and washed by deionized water and isopropanol and dried at 80°C for 24 hours. High mass loading $Zn_{0.25}V_2O_5$ cathodes were fabricated by a vacuum infiltration method. The aqueous mixture of CNT suspension (Canrd New Energy Technology Co. Ltd.) and $Zn_{0.25}V_2O_5$ powder (2:8 by weight) was sonicated for 10 hours and then vacuum-infiltrated. The freestanding cathodes were dried at 80°C for 12 hours.

Electrochemical tests

All Zn metal aqueous batteries (symmetric Zn batteries, Zn/Ti batteries, and Zn/ZnVO full batteries) were assembled in atmospheric environment using pouch-type battery model. Glass fiber membrane (GF/A, Whatman) or cellulose membrane (Shanghai Xinya Purification Equipment Co. Ltd.) was used as separator. LAND battery cycler and Solartron Analytical Electrochemical Workstation were used for the electrochemical measurements. Zn CE was measured in Zn/Ti cells. A fixed amount Zn (6 mA·hour cm^{-2}) was plated on Ti electrode and then stripped back under different current densities until the cutoff voltage increased to 1 V. Ultrathin Zn foils (20 μm; Runde Metal Co. Ltd.) were used in symmetric Zn/Zn and Zn/ZnVO tests. Long-term cycle life-span tests of Zn/ZnVO full cells were cycled at 4 mA cm^{-2} within a voltage range of 0.2 to 1.6 V versus Zn^{2+}/Zn.

Computational methodology

All DFT calculations were performed at the GFN1-xTB level using the xTB program, version 6.3.2. The geometry optimizations were calculated with periodic boundary conditions, while the frequency was calculated without periodic boundary conditions.

For electronic self-consistent calculations, geometry optimizations, and frequency calculations, the convergence tolerance is set as follows: integral cutoff = 0.25×10^2, Broyden damping = 0.40, and the accuracy = 1.0.

The free energy change for different steps was determined as follows

$$\Delta G_1 = E_{\text{bind}} - E_{\text{C3N4}} - 4 \times E_{\text{ZnSO4}} + \Delta E_{\text{ZPE}} + \Delta H_{0\rightarrow 300\text{K}} - T\Delta S$$

$$\Delta G_2 = E_{\text{ads}} - E_{\text{slab}} - E_{\text{bind}} + \Delta E_{\text{ZPE}} + \Delta H_{0\rightarrow 300\text{K}} - T\Delta S$$

Here, E_{bind}, E_{C3N4}, E_{ZnSO4}, E_{ads}, and E_{slab} are the electronic energy of g-C_3N_4 and $ZnSO_4$ binding state, g-C_3N_4 single state, $ZnSO_4$ single state, adsorption state, and Zn slab. ΔE_{ZPE}, $\Delta H_{0\rightarrow 300\text{K}}$, and ΔS are zero-point energy change, thermal correction change from 0 to 300 K, and entropy change, which were also obtained through the xTB program, version 6.3.2.

SUPPLEMENTARY MATERIALS

Supplementary material for this article is available at https://science.org/doi/10.1126/sciadv.abl3752

REFERENCES AND NOTES

1. J. F. Parker, C. N. Chervin, I. R. Pala, M. Machler, M. F. Burz, J. W. Long, D. R. Rolison, Rechargeable nickel–3D zinc batteries: An energy-dense, safer alternative to lithium-ion. *Science* **356**, 415–418 (2017).
2. W. Sun, F. Wang, B. Zhang, M. Zhang, V. Küpers, X. Ji, C. Theile, P. Bieker, K. Xu, C. Wang, M. Winter, A rechargeable zinc-air battery based on zinc peroxide chemistry. *Science* **371**, 46–51 (2021).
3. J. W. Choi, D. Aurbach, Promise and reality of post-lithium-ion batteries with high energy densities. *Nat. Rev. Mater.* **1**, 16013 (2016).
4. Y. Tian, G. Zeng, A. Rutt, T. Shi, H. Kim, J. Wang, J. Koettgen, Y. Sun, B. Ouyang, T. Chen, Z. Lun, Z. Rong, K. Persson, G. Ceder, Promises and challenges of next-generation "Beyond Li-ion" batteries for electric vehicles and grid decarbonization. *Chem. Rev.* **121**, 1623–1669 (2021).
5. M. Li, J. Lu, X. Ji, Y. Li, Y. Shao, Z. Chen, C. Zhong, K. Amine, Design strategies for nonaqueous multivalent-ion and monovalent-ion battery anodes. *Nat. Rev. Mater.* **5**, 276–294 (2020).
6. M.-C. Lin, M. Gong, B. Lu, Y. Wu, D. Y. Wang, M. Guan, M. Angell, C. Chen, J. Yang, B. J. Hwang, H. Dai, An ultrafast rechargeable aluminium-ion battery. *Nature* **520**, 324–328 (2015).
7. P. Bai, J. Li, F. R. Brushett, M. Z. Bazant, Transition of lithium growth mechanisms in liquid electrolytes. *Energ. Environ. Sci.* **9**, 3221–3229 (2016).
8. Q. Yang, Q. Li, Z. Liu, D. Wang, Y. Guo, X. Li, Y. Tang, H. Li, B. Dong, C. Zhi, Dendrites in Zn-based batteries. *Adv. Mater.* **32**, 2001854 (2020).
9. X.-B. Cheng, R. Zhang, C.-Z. Zhao, Q. Zhang, Toward safe lithium metal anode in rechargeable batteries: A review. *Chem. Rev.* **117**, 10403–10473 (2017).
10. C. Fang, J. Li, M. Zhang, Y. Zhang, F. Yang, J. Z. Lee, M. H. Lee, J. Alvarado, M. A. Schroeder, Y. Yang, B. Lu, N. Williams, M. Ceja, L. Yang, M. Cai, J. Gu, K. Xu, X. Wang, Y. S. Meng, Quantifying inactive lithium in lithium metal batteries. *Nature* **572**, 511–515 (2019).
11. Y. Fang, S. L. Zhang, Z.-P. Wu, D. Luan, X. W. Lou, A highly stable lithium metal anode enabled by Ag nanoparticle–embedded nitrogen-doped carbon macroporous fibers. *Sci. Adv.* **7**, eabg3626 (2021).
12. W. Zhang, H. L. Zhuang, L. Fan, L. Gao, Y. Lu, A "cation-anion regulation" synergistic anode host for dendrite-free lithium metal batteries. *Sci. Adv.* **4**, eaar4410 (2018).
13. Q. Zhao, S. Stalin, L. A. Archer, Stabilizing metal battery anodes through the design of solid electrolyte interphases. *Joule* **5**, 1119–1142 (2021).
14. W. Zhang, S. Zhang, L. Fan, L. Gao, X. Kong, S. Li, J. Li, X. Hong, Y. Lu, Tuning the LUMO energy of an organic interphase to stabilize lithium metal batteries. *ACS Energy Lett.* **4**, 644–650 (2019).
15. K. Xu, Electrolytes and interphases in Li-ion batteries and beyond. *Chem. Rev.* **114**, 11503–11618 (2014).
16. W. Zhang, Q. Wu, J. Huang, L. Fan, Z. Shen, Y. He, Q. Feng, G. Zhu, Y. Lu, Colossal granular lithium deposits enabled by the grain-coarsening effect for high-efficiency lithium metal full batteries. *Adv. Mater.* **32**, 2001740 (2020).
17. W. Zhang, Z. Shen, S. Li, L. Fan, X. Wang, F. Chen, X. Zang, T. Wu, F. Ma, Y. Lu, Engineering wavy-nanostructured anode interphases with fast ion transfer kinetics: Toward practical Li-metal full batteries. *Adv. Funct. Mater.* **30**, 2003800 (2020).
18. L. Cao, D. Li, T. Pollard, T. Deng, B. Zhang, C. Yang, L. Chen, J. Vatamanu, E. Hu, M. J. Hourwitz, L. Ma, M. Ding, Q. Li, S. Hou, K. Gaskell, J. T. Fourkas, X. Q. Yang, K. Xu, O. Borodin, C. Wang, Fluorinated interphase enables reversible aqueous zinc battery chemistries. *Nat. Nanotechnol.* **16**, 902–910 (2021).
19. Y. Gao, Z. Yan, J. L. Gray, X. He, D. Wang, T. Chen, Q. Huang, Y. C. Li, H. Wang, S. H. Kim, T. E. Mallouk, D. Wang, Polymer–inorganic solid–electrolyte interphase for stable lithium metal batteries under lean electrolyte conditions. *Nat. Mater.* **18**, 384–389 (2019).
20. J. Zhou, M. Xie, F. Wu, Y. Mei, Y. Hao, R. Huang, G. Wei, A. Liu, L. Li, R. Chen, Ultrathin surface coating of nitrogen-doped graphene enables stable zinc anodes for aqueous zinc-ion batteries. *Adv. Mater.* **33**, 2101649 (2021).
21. J. Zheng, Q. Zhao, T. Tang, J. Yin, C. D. Quilty, G. D. Renderos, X. Liu, Y. Deng, L. Wang, D. C. Bock, C. Jaye, D. Zhang, E. S. Takeuchi, K. J. Takeuchi, A. C. Marschilok, L. A. Archer, Reversible epitaxial electrodeposition of metals in battery anodes. *Science* **366**, 645–648 (2019).
22. T. Foroozan, V. Yurkiv, S. Sharifi-Asl, R. Rojaee, F. Mashayek, R. Shahbazian-Yassar, Non-dendritic Zn electrodeposition enabled by zincophilic graphene substrates. *ACS Appl. Mater. Interfaces* **11**, 44077–44089 (2019).
23. D. Lin, Y. Liu, Y. Cui, Reviving the lithium metal anode for high-energy batteries. *Nat. Nanotechnol.* **12**, 194–206 (2017).
24. L. Ma, M. A. Schroeder, O. Borodin, T. P. Pollard, M. S. Ding, C. Wang, K. Xu, Realizing high zinc reversibility in rechargeable batteries. *Nat. Energy* **5**, 743–749 (2020).
25. J. Zhi, S. Li, M. Han, P. Chen, Biomolecule-guided cation regulation for dendrite-free metal anodes. *Sci. Adv.* **6**, eabb1342 (2020).
26. L. Addadi, S. Weiner, Control and design principles in biological mineralization. *Angew. Chem. Int. Ed.* **31**, 153–169 (1992).

27. P. J. M. Smeets, K. R. Cho, R. G. E. Kempen, N. A. J. M. Sommerdijk, J. J. De Yoreo, Calcium carbonate nucleation driven by ion binding in a biomimetic matrix revealed by in situ electron microscopy. *Nat. Mater.* **14**, 394–399 (2015).
28. L.-B. Mao, H. L. Gao, H. B. Yao, L. Liu, H. Cölfen, G. Liu, S. M. Chen, S. K. Li, Y. X. Yan, Y. Y. Liu, S. H. Yu, Synthetic nacre by predesigned matrix-directed mineralization. *Science* **354**, 107–110 (2016).
29. S. C. Glotzer, M. J. Solomon, Anisotropy of building blocks and their assembly into complex structures. *Nat. Mater.* **6**, 557–562 (2007).
30. D. Chao, W. Zhou, F. Xie, C. Ye, H. Li, M. Jaroniec, S.-Z. Qiao, Roadmap for advanced aqueous batteries: From design of materials to applications. *Sci. Adv.* **6**, eaba4098 (2020).
31. G. G. Yadav, J. W. Gallaway, D. E. Turney, M. Nyce, J. Huang, X. Wei, S. Banerjee, Regenerable Cu-intercalated MnO_2 layered cathode for highly cyclable energy dense batteries. *Nat. Commun.* **8**, 14424 (2017).
32. H. Pan, Y. Shao, P. Yan, Y. Cheng, K. S. Han, Z. Nie, C. Wang, J. Yang, X. Li, P. Bhattacharya, K. T. Mueller, J. Liu, Reversible aqueous zinc/manganese oxide energy storage from conversion reactions. *Nat. Energy* **1**, 16039 (2016).
33. Z. Hong, Z. Ahmad, V. Viswanathan, Design principles for dendrite suppression with porous polymer/aqueous solution hybrid electrolyte for Zn metal anodes. *ACS Energy Lett.* **5**, 2466–2474 (2020).
34. V. Verma, S. Kumar, W. Manalastas, M. Srinivasan, Undesired reactions in aqueous rechargeable zinc ion batteries. *ACS Energy Lett.* **6**, 1773–1785 (2021).
35. B. Tang, L. Shan, S. Liang, J. Zhou, Issues and opportunities facing aqueous zinc-ion batteries. *Energ. Environ. Sci.* **12**, 3288–3304 (2019).
36. J. Zheng, L. A. Archer, Controlling electrochemical growth of metallic zinc electrodes: Toward affordable rechargeable energy storage systems. *Sci. Adv.* **7**, eabe0219 (2021).
37. I. Dozov, E. Paineau, P. Davidson, K. Antonova, C. Baravian, I. Bihannic, L. J. Michot, Electric-field-induced perfect anti-nematic order in isotropic aqueous suspensions of a natural beidellite clay. *J. Phys. Chem. B.* **115**, 7751–7765 (2011).
38. S. Cetindag, B. Tiwari, D. Zhang, Y. K. Yap, S. Kim, J. W. Shan, Surface-charge effects on the electro-orientation of insulating boron-nitride nanotubes in aqueous suspension. *J. Colloid Interface Sci.* **505**, 1185–1192 (2017).
39. A. Dazzi, C. B. Prater, AFM-IR: Technology and applications in nanoscale infrared spectroscopy and chemical imaging. *Chem. Rev.* **117**, 5146–5173 (2017).
40. T. Liu, L. Lin, X. Bi, L. Tian, K. Yang, J. Liu, M. Li, Z. Chen, J. Lu, K. Amine, K. Xu, F. Pan, In situ quantification of interphasial chemistry in Li-ion battery. *Nat. Nanotechnol.* **14**, 50–56 (2019).
41. X. Zeng, J. Mao, J. Hao, J. Liu, S. Liu, Z. Wang, Y. Wang, S. Zhang, T. Zheng, J. Liu, P. Rao, Z. Guo, Electrolyte design for in situ construction of highly Zn^{2+}-conductive solid electrolyte interphase to enable high-performance aqueous Zn-ion batteries under practical conditions. *Adv. Mater.* **33**, 2007416 (2021).
42. D. Kundu, B. D. Adams, V. Duffort, S. H. Vajargah, L. F. Nazar, A high-capacity and long-life aqueous rechargeable zinc battery using a metal oxide intercalation cathode. *Nat. Energy* **1**, 16119 (2016).
43. W. Yang, X. Du, J. Zhao, Z. Chen, J. Li, J. Xie, Y. Zhang, Z. Cui, Q. Kong, Z. Zhao, C. Wang, Q. Zhang, G. Cui, Hydrated eutectic electrolytes with ligand-oriented solvation shells for long-cycling zinc-organic batteries. *Joule* **4**, 1557–1574 (2020).
44. H. Qiu, X. Du, J. Zhao, Y. Wang, J. Ju, Z. Chen, Z. Hu, D. Yan, X. Zhou, G. Cui, Zinc anode-compatible in-situ solid electrolyte interphase via cation solvation modulation. *Nat. Commun.* **10**, 5374 (2019).
45. D. Yuan, J. Zhao, H. Ren, Y. Chen, R. Chua, E. T. J. Jie, Y. Cai, E. Edison, W. Manalastas Jr., M. W. Wong, M. Srinivasan, Anion texturing towards dendrite-free Zn anode for aqueous rechargeable batteries. *Angew. Chem. Int. Ed.* **60**, 7213–7219 (2021).
46. G. Wang, B. Kohn, U. Scheler, F. Wang, S. Oswald, M. Löffler, D. Tan, P. Zhang, J. Zhang, X. Feng, A high-voltage, dendrite-free, and durable Zn–graphite battery. *Adv. Mater.* **32**, 1905681 (2020).
47. N. Zhang, F. Cheng, Y. Liu, Q. Zhao, K. Lei, C. Chen, X. Liu, J. Chen, Cation-deficient spinel $ZnMn_2O_4$ cathode in $Zn(CF_3SO_3)_2$ electrolyte for rechargeable aqueous Zn-ion battery. *J. Am. Chem. Soc.* **138**, 12894–12901 (2016).
48. X. Guo, Z. Zhang, J. Li, N. Luo, G. L. Chai, T. S. Miller, F. Lai, P. Shearing, D. J. L. Brett, D. Han, Z. Weng, G. He, I. P. Parkin, Alleviation of dendrite formation on zinc anodes via electrolyte additives. *ACS Energy Lett.* **6**, 395–403 (2021).
49. S. Chen, R. Lan, J. Humphreys, S. Tao, Salt-concentrated acetate electrolytes for a high voltage aqueous Zn/MnO_2 battery. *Energy Stor. Mater.* **28**, 205–215 (2020).
50. Y. Jin, K. S. Han, Y. Shao, M. L. Sushko, J. Xiao, H. Pan, J. Liu, Stabilizing zinc anode reactions by polyethylene oxide polymer in mild aqueous electrolytes. *Adv. Funct. Mater.* **30**, 2003932 (2020).
51. H. Yang, Z. Chang, Y. Qiao, H. Deng, X. Mu, P. He, H. Zhou, Constructing a super-saturated electrolyte front surface for stable rechargeable aqueous zinc batteries. *Angew. Chem. Int. Ed.* **59**, 9377–9381 (2020).
52. J. Hao, B. Li, X. Li, X. Zeng, S. Zhang, F. Yang, S. Liu, D. Li, C. Wu, Z. Guo, An in-depth study of Zn metal surface chemistry for advanced aqueous Zn-ion batteries. *Adv. Mater.* **32**, 2003021 (2020).
53. Z. Zhao, J. Zhao, Z. Hu, J. Li, J. Li, Y. Zhang, C. Wang, G. Cui, Long-life and deeply rechargeable aqueous Zn anodes enabled by a multifunctional brightener-inspired interphase. *Energ. Environ. Sci.* **12**, 1938–1949 (2019).
54. N. Zhang, S. Huang, Z. Yuan, J. Zhu, Z. Zhao, Z. Niu, Direct self-assembly of MXene on Zn anodes for dendrite-free aqueous zinc-ion batteries. *Angew. Chem. Int. Ed.* **60**, 2861–2865 (2021).
55. X. Liu, F. Yang, W. Xu, Y. Zeng, J. He, X. Lu, Zeolitic imidazolate frameworks as Zn^{2+} modulation layers to enable dendrite-free Zn anodes. *Adv. Sci.* **7**, 2002173 (2020).
56. Y. Cui, Q. Zhao, X. Wu, X. Chen, J. Yang, Y. Wang, R. Qin, S. Ding, Y. Song, J. Wu, K. Yang, Z. Wang, Z. Mei, Z. Song, H. Wu, Z. Jiang, G. Qian, L. Yang, F. Pan, An interface-bridged organic–inorganic layer that suppresses dendrite formation and side reactions for ultra-long-life aqueous zinc metal anodes. *Angew. Chem. Int. Ed.* **59**, 16594–16601 (2020).
57. L. Kang, M. Cui, F. Jiang, Y. Gao, H. Luo, J. Liu, W. Liang, C. Zhi, Nanoporous $CaCO_3$ coatings enabled uniform Zn ztripping/plating for long-life zinc rechargeable aqueous batteries. *Adv. Energy Mater.* **8**, 1801090 (2018).
58. Z. Cao, X. Zhu, D. Xu, P. Dong, M. O. L. Chee, X. Li, K. Zhu, M. Ye, J. Shen, Eliminating Zn dendrites by commercial cyanoacrylate adhesive for zinc ion battery. *Energy Stor. Mater.* **36**, 132–138 (2021).
59. S.-B. Wang, Q. Ran, R. Q. Yao, H. Shi, Z. Wen, M. Zhao, X. Y. Lang, Q. Jiang, Lamella-nanostructured eutectic zinc–aluminum alloys as reversible and dendrite-free anodes for aqueous rechargeable batteries. *Nat. Commun.* **11**, 1634 (2020).
60. A. Bayaguud, X. Luo, Y. Fu, C. Zhu, Cationic surfactant-type electrolyte additive enables three-dimensional dendrite-free zinc anode for stable zinc-ion batteries. *ACS Energy Lett.* **5**, 3012–3020 (2020).
61. Y. Zeng, X. Zhang, R. Qin, X. Liu, P. Fang, D. Zheng, Y. Tong, X. Lu, Dendrite-free zinc deposition induced by multifunctional CNT frameworks for stable flexible Zn-ion batteries. *Adv. Mater.* **31**, 1903675 (2019).
62. Z. Kang, C. Wu, L. Dong, W. Liu, J. Mou, J. Zhang, Z. Chang, B. Jiang, G. Wang, F. Kang, C. Xu, 3D porous copper skeleton supported zinc anode toward high capacity and long cycle life zinc ion batteries. *ACS Sustain. Chem. Eng.* **7**, 3364–3371 (2019).
63. Y. Zhou, X. Wang, X. Shen, Y. Shi, C. Zhu, S. Zeng, H. Xu, P. Cao, Y. Wang, J. Di, Q. Li, 3D confined zinc plating/stripping with high discharge depth and excellent high-rate reversibility. *J. Mater. Chem. A* **8**, 11719–11727 (2020).
64. C. Shen, X. Li, N. Li, K. Xie, J. G. Wang, X. Liu, B. Wei, Graphene-boosted, high-performance aqueous Zn-ion battery. *ACS Appl. Mater. Interfaces* **10**, 25446–25453 (2018).

Acknowledgments: We thank F. Chen and X. Ding (Department of Chemistry, Zhejiang University) for SEM/TEM analysis and J. Guo (Cryo-Electron Microscopy, Zhejiang University) for FIB characterization and 3D reconstruction. **Funding:** This work was supported by Natural Science Foundation of China (22022813 and 21878268), National Key R&D Program of China (2018YFA0209600), and Leading Innovative and Entrepreneur Team Introduction Program of Zhejiang (2019R01006). The collaborative project was supported by a grant from the Cornell-Zhejiang University Seed funding program. **Author contributions:** Y.L. and L.A.A. directed the research. W.Z., Q.Z., Y.L., and L.A.A. conceived the idea, designed the experiments, and wrote the manuscript. W.Z., Q.Z., and Z.S. performed the electrodeposition, electrochemical measurements, and characterizations. L.F. carried out the XRD investigation. Y.H. and S.Z. performed the DFT calculations. **Competing interests:** L.A.A. is a founder and member of the board of directors of NOHMs Technologies. This company develops and commercializes electrolytes for Li-ion and Li-sulfur battery technology. The authors declare that they have no other competing interests. **Data and materials availability:** All data needed to evaluate the conclusions in the paper are present in the paper or the Supplementary Materials.

Submitted 9 July 2021
Accepted 13 October 2021
Published 1 December 2021
10.1126/sciadv.abl3752